Article

Electrochemical Investigation of Lithium Perchlorate-Doped Polypyrrole Growing on Titanium Substrate

Yibing Xie [1,2],* , Jing Xu [3] , Lu Lu [4] and Chi Xia [5]

1   School of Chemistry and Chemical Engineering, Southeast University, Nanjing 211189, China
2   Suzhou Research Institute, Southeast University, Suzhou 215123, China
3   College of Ecology and Resource Engineering, Wuyi University, Wuyishan 354300, China
4   School of Intelligent and Automotive Engineering, Wuxi Vocational Institute of Commerce, Wuxi 214153, China
5   Institute of Shandong Non-Metallic Materials, Jinan 250031, China
*   Correspondence: ybxie@seu.edu.cn

Abstract: Lithium perchlorate-doped polypyrrole growing on titanium substrate ($LiClO_4$-PPy/Ti) has been fabricated to act as electroactive electrode material for feasible electrochemical energy storage. A theoretical and experimental investigation is adopted to disclose the conductivity, electroactivity properties and interfacial interaction-dependent capacitance of $LiClO_4$-PPy/Ti electrode. The experimental measurement results disclose that $LiClO_4$-PPy/Ti reveals lower ohmic resistance ($0.2226\ \Omega\ cm^{-2}$) and charge transfer resistance ($2116\ \Omega\ cm^{-2}$) to exhibit higher electrochemical conductivity, a more reactive surface, and feasible ion diffusion to present higher double-layer capacitance ($0.1930\ mF\ cm^{-2}$) rather than $LiClO_4$/Ti ($0.3660\ \Omega\ cm^{-2}$, $65,250\ \Omega\ cm^{-2}$, $0.0334\ mF\ cm^{-2}$). $LiClO_4$-PPy/Ti reveals higher Faradaic capacitance caused by the reversible doping and dedoping process of perchlorate ion on PPy than the electrical double-layer capacitance of $LiClO_4$/Ti caused by the reversible adsorption and desorption process of the $LiClO_4$ electrolyte on Ti. Theoretical simulation calculation results prove that a more intensive electrostatic interaction of pyrrole N···Ti ($2.450\ Å$) in $LiClO_4$-PPy/Ti rather than perchlorate O···Ti ($3.537\ Å$) in $LiClO_4$/Ti. $LiClO_4$-PPy/Ti exhibits higher density of states (57.321 electrons/eV) at Fermi energy and lower HOMO-LUMO molecule orbital energy gap ($0.032\ eV$) than $LiClO_4$/Ti (9.652 electrons/eV, $0.340\ eV$) to present the enhanced electronic conductivity. $LiClO_4$-PPy/Ti also exhibits a more declined interface energy (-1.461×10^4) than $LiClO_4$/Ti ($-5.202 \times 10^3\ eV$) to present the intensified interfacial interaction. $LiClO_4$-PPy/Ti accordingly exhibits much higher specific capacitances of 0.123~$0.0122\ mF\ cm^{-2}$ at current densities of 0.01~$0.10\ mA\ cm^{-2}$ rather than $LiClO_4$/Ti (0.010~$0.0095\ mF\ cm^{-2}$, presenting superior electroactivity and electrochemical capacitance properties. $LiClO_4$-PPy/Ti could well act as the electroactive supercapacitor electrode for feasible energy storage.

Keywords: lithium perchlorate doping polypyrrole; titanium substrate; electrochemical capacitance; interfacial interaction; simulation calculation

1. Introduction

The electrochemical behaviors and performances of energy storage devices are related to the electrode and electrolyte materials as well as their interfacial interaction [1–3]. In addition, the electrode substrate materials are also related to the properties of functional electrodes. The electrochemical capacity and mechanical stability are most concerned for the electrodes of energy storage devices. These electrode materials mainly involve the various graphite carbon, conductive polymers, transition metal sulfates or oxides, and their composites [4–7]. In particular, the conductive polymers become suitable supercapacitor electrode materials for flexible energy storage [8,9]. The electrical conductive materials, such as carbon fiber, graphene, graphite carbon, titanium, and so on, have been used to prepare the energy storage electrodes [10–12]. They could act as the multifunctional roles,

such as the electrode substrate, current collector, and electrode. However, the contradictory behaviors of these substrate materials also emerged in respect to the electrochemical activity and electrochemical stability. For example, titanium metal could resist the chemical and electrochemical corrosion in neutral, alkaline, and even acidic conditions [13]. Titanium keeps the chemical and electrochemical stability in a certain degree, and is applied to electrode material as well as electrode-supporting material [14–17]. The structure-adjusted titanium, such as titanium sheet, titanium mesh, and titanium foam with high electro-chemical stability, can be used to support various electroactive materials [18–21]. On the other hand, titanium metal also behaves the relatively low electrochemical activity due to the passivation layer of titanium oxides on the surface [22]. Surface modification us-ing conductive polymers is a useful method to Improve the electrochemical activity of titanium. The Ti metal sheet can act as the electrode substrate. The conductive polymers usually includes polyaniline, polypyrrole, and polythiophene, which have been used to act as electroactive materials for the supercapacitor electrode application [23]. The different electroactive materials can be coated on Ti substrate to form functional electrodes. The polypyrrole (pPy) has been electrodeposited on Ti substrate to form pPy/Ti electrode through cyclic voltammetry polymerization process [24]. The polyaniline (PANI) has been electrodeposited and coated on Ti substrate to form PANI/Ti electrode through a pulse potentiostatic polymerization process [25]. These conductive polymers could conduct the reversible ion doping–dedoping process to provide superior capacitance [26–28]. The interfacial bonding strength between the doped conductive polymers and metal substrates is related to the electrochemical energy storage performance [29]. In addition, the reactive electrolytes also influence the electrical double-layer capacitance due to the interfacial adsorption on metal substrates and the Faradaic capacitance due to the ion doping state of conductive polymers. In previous studies, the system of a lithium perchlorate electrolyte and polypyrrole has been attempted for various applications in different areas [30,31]. However, the interfacial interaction between lithium perchlorate doping polypyrrole and metal titanium substrate is still sparsely investigated [32].

This study focuses on disclosing the promotion effect of electroactive polypyrrole on the electrochemical properties of lithium perchlorate interacting with titanium sub-strate. The polypyrrole is used as the typical conductive polymer material, and a metal titanium sheet is used as the stable substrate material. The titanium sheet has chemical and electrochemical stability to resist the electrochemical corrosion to act as a suitable current collector. The polypyrrole growing on titanium substrate (PPy/Ti) is designed as the supercapacitor electrode in the application of electrochemical energy storage, which is prepared through the electrochemical polymerization process. The lithium perchlorate ($LiClO_4$) is used as a neural electrolyte to study the electrical double-layer capacitance of titanium metal substrate and the Faradaic capacitance of polypyrrole. The interfacial inter-action is intensively considered between the $LiClO_4$ electrolyte and the PPy/Ti electrode when the electrochemical behavior is investigated for $LiClO_4$-Ppy/Ti. The electrochemical performances are fully evaluated through cyclic voltammetry, electrochemical impedance spectrum, and galvanostatic charge/discharge measurements. The theoretical simulation calculation has been applied to disclose the atomic charge distribution, electrostatic poten-tial, and interfacial affinity of $LiClO_4$-PPy/Ti, which could lead to a better understanding of capacitance performance.

2. Results and Discussion

2.1. Microstructure and Morphology Characterization

Figure 1A–D shows SEM images of Ti and PPy/Ti. The Ti sheet substrate reveals the uniquely complete surface structure without any crack. The chemical polishing treatment could lead to forming the uniform metal surface. Comparatively, PPy/Ti revels the com-pact covering layer of PPy film supported on the Ti sheet. The PPy also is composed of the aggregating particles, forming uniquely complete film structure without any crack. Concerning the surface microstructure, the Ti sheet shows smooth surface and PPy/Ti

shows rough surface. The insert in Figure 1D shows the cross-section SEM image of PPy/Ti. The PPy covered on the surface of the Ti substrate exhibits a close-packing film. The morphology, microstructure, and thickness of such PPy film could be adjusted by modulating the electropolymerization reaction parameters in the CV electrodeposition process. This study focuses on the interfacial interaction between PPy film and Ti substrate, which is related to the microstructure of PPy. It is believed that PPy/Ti could conduct more feasible ion diffusion and doping reaction in the presence of lithium perchlorate in comparison the ion adsorption of PPy/Ti.
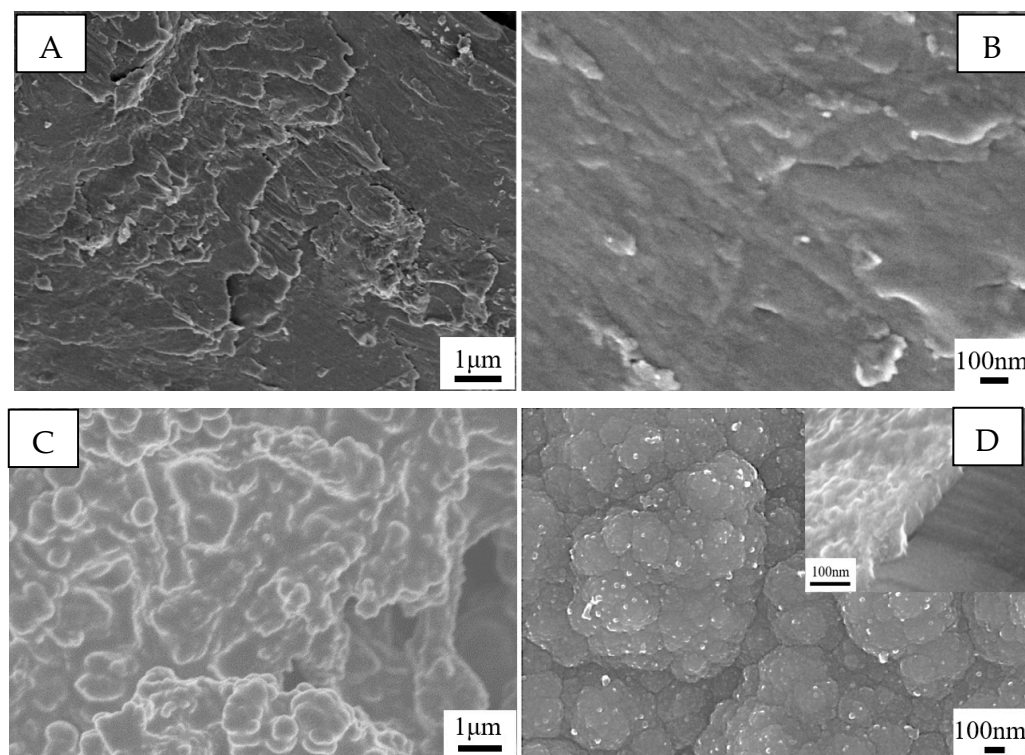

Figure 1. (**A**) SEM image and (**B**) magnified SEM image of Ti; (**C**) SEM image of PPy/Ti; and (**D**) magnified SEM image and cross-section SEM image of PPy/Ti.

Figure 2A shows the XRD pattern of the titanium sheet substrate. Concerning the titanium sheet, the distinct characteristic diffraction peaks at 2θ of 35.1°, 38.5°, 40.3°, 53.1°, 63.1°, 70.8°, 76.3°, 77.5°, and 82.3° correspond to the respective crystal planes of (100), (002), (101), (102), (110), (103), (112), (201), and (202) [33]. The titanium sheet involves the close-packed hexagonal crystal phase structure, which is acted as stable metal substrate. Figure 2B shows the Raman spectrum of the Ti substrate. The Ti substrate does not reveal any characteristic Raman peaks in full wavenumber range due to the absence of electronic transition-relaxation of crystal lattice Ti atoms at 785 nm excitation photon energy. Figure 2C shows the Raman spectrum of PPy/Ti synthesized in this study. The characteristic Raman peaks of PPy/Ti are observed at 983 and 1050 cm^{-1}, with a broad band of 1340–1410 cm^{-1} and 1580 cm^{-1}, which are assigned to C–H ring deformation vibration, C–N stretching vibration, and C=C aromatic stretching vibration, respectively. The characteristic Raman peak position of the literature-reported PPy is located at 980, 1040, 1314–1410 cm^{-1}, and 1597 cm^{-1} [34]. The characteristic Raman peaks of PPy are well-matched between this study-formed PPy/Ti and the literature-reported PPy. Therefore, the Raman spectrum analysis result could well confirm the formation of PPy in the as-prepared PPy/Ti electrode in this study. Figure 2D shows the FTIR spectrum of PPy/Ti. The characteristic peaks at 1540, 1480, 1190, and 1040 cm^{-1} were ascribed to C=C double bond stretching vibration, C-C single bond stretching vibration, C-N single bond stretching vibration, and N-H

in-plane bending vibration. The characteristic peaks at 912, 768, 742, and 675 cm^{-1} are ascribed to the C-H out-of-plane bending vibration. The observation of the C=C double bond, C-C single bond, and C-N single bond could be ascribed to the formation of PPy. Accordingly, PPy fully grew on the Ti substate to form PPy/Ti through the electrochemical polymerization and deposition process.
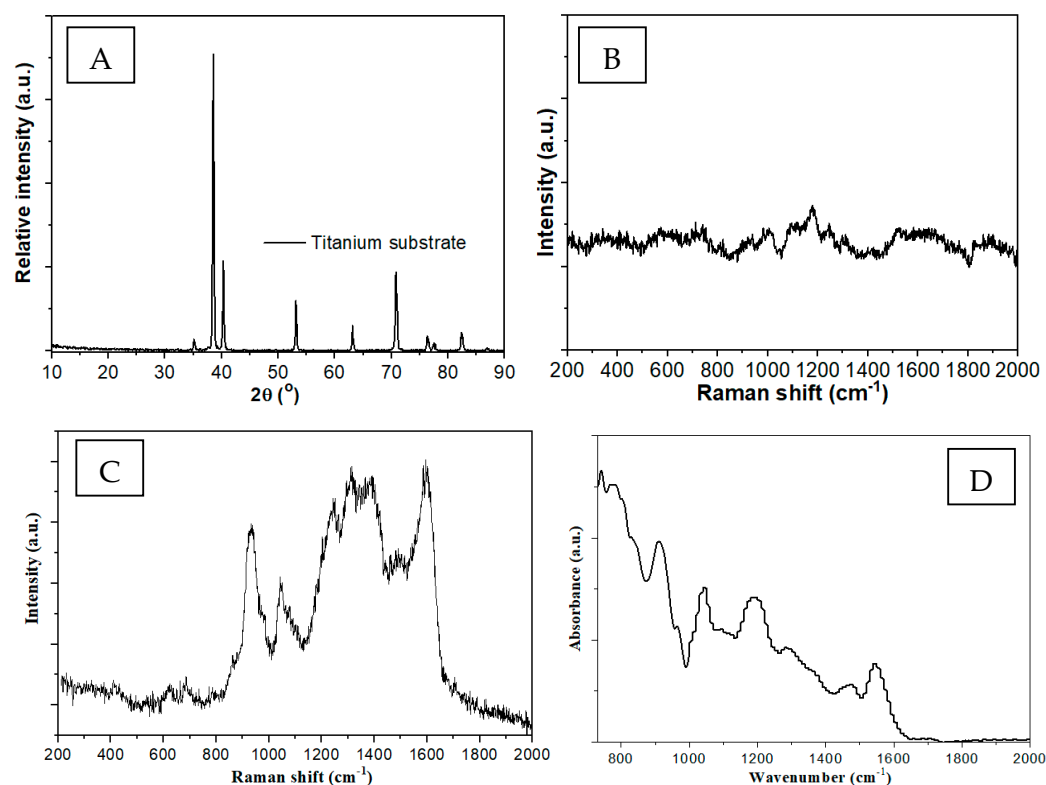

Figure 2. (A) XRD pattern and **(B)** Raman spectrum of Ti substrate; **(C)** Raman spectrum of PPy/Ti; and **(D)** FTIR spectrum of PPy/Ti.

2.2. Electrochemical Properties

The CV curves can be used to calculate the CV-based capacitance (C_{CV}, mF cm^{-2}) using Equation (1). The GCD curves can be used to calculate the GCD-based capacitance (C_{GCD}, mF cm^{-2}) using Equation (2).

$$C_{CV} = i/v = [(\int_{V_c}^{V_a} i(v) * dv)/(V_a - V_c)]/v = [\frac{1}{2}(\oint i(v) * dv)/\Delta V]/v \tag{1}$$

$$C_{GCD} = \frac{I * t}{\Delta V} \tag{2}$$

where: V_a, upper potential; V_c, lower potential; $i(v)$, response current density (mA cm^{-2}); v, potential sweep rate (V s^{-1}); I, discharge current density (mA cm^{-2}); t, discharge time (s); and ΔV, potential window (V).

Figure 3A,B shows the CV curves of LiClO$_4$/Ti and LiClO$_4$-PPy/Ti at scan rates of 5~200 mV s^{-1} and the potential range of 0~0.8 V versus saturated calomel electrode (SCE) in 1.0 M LiClO$_4$ electrolyte solution. The CV curves of LiClO$_4$/Ti demonstrate the rectangle-like shape to present electrical double-layer capacitance due to the reversible adsorption–desorption of LiClO$_4$ electrolyte ion on the Ti substrate. The oxidation potential of Ti^{2+}/Ti is −1.39 V versus SCE. This means that the electrochemical oxidation of Ti is unlikely to occur in the potential range of 0~0.8 V versus SCE, presenting the high electrochemical stability of the Ti substrate in LiClO$_4$ electrolyte. Comparatively, the CV curves of LiClO$_4$-PPy/Ti exhibit an obviously deviated rectangle shape in the potential

range of 0~0.8 V, presenting the polarization effect. The redox potential of PPy is around 0.5 V versus SCE [35]. LiClO$_4$-PPy conducts reversible ClO$_4^-$ doping-dedoping reaction which contributes to the Faradaic capacitance performance.
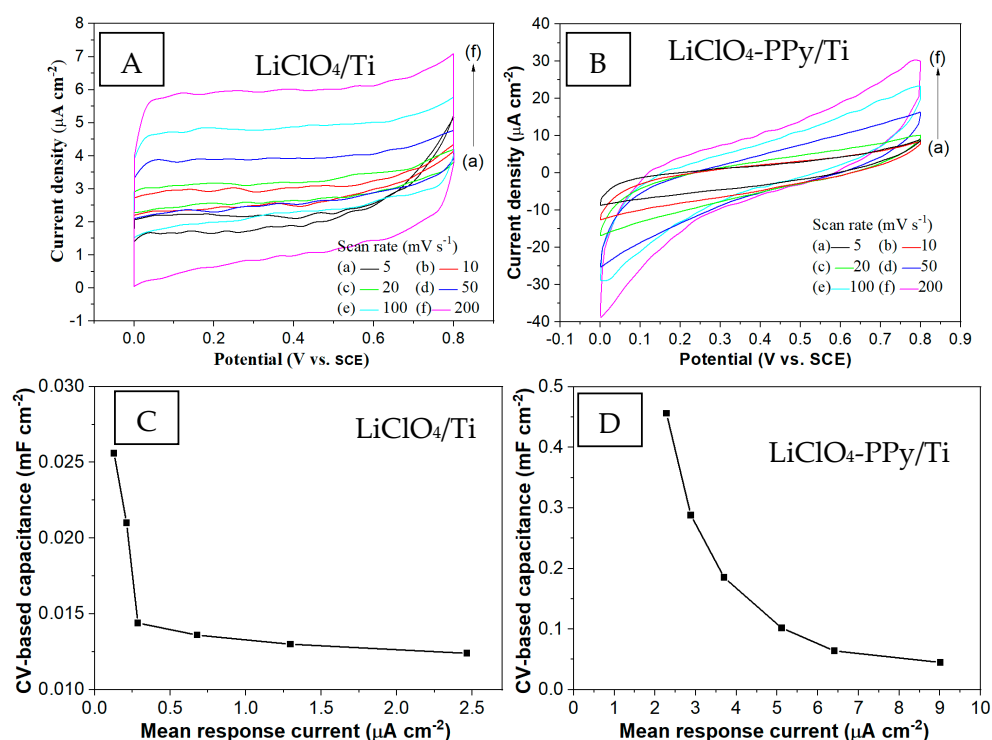

Figure 3. (**A,B**) CV curves and (**C,D**) CV-based capacitance curves of LiClO$_4$/Ti and LiClO$_4$-PPy/Ti at scan rates of 5~200 mV s^{-1} in 1.0 M LiClO$_4$ electrolyte solution.

Figure 3C,D shows CV-based capacitance curves of LiClO$_4$/Ti and LiClO$_4$-PPy/Ti. When the CV cures of LiClO$_4$/Ti and LiClO$_4$-PPy/Ti conduct the scan rate increasing from 5 to 200 mV s^{-1}, their mean response current increases from 0.13 to 2.47 μA cm^{-2} and from 2.28 to 9.011 μA cm^{-2}, respectively. The CV-based capacitance decreases from 0.0256 to 0.0124 mF cm^{-2} and from 0.456–0.045 mF cm^{-2}, respectively. In comparison with LiClO$_4$/Ti, LiClO$_4$-PPy/Ti exhibits a much higher mean response current and specific capacitance performance at the same scan rate, presenting its superior electrochemical activity in the neutral LiClO$_4$ electrolyte. The oxidation potential of Ti^{2+}/Ti is 1.39 V versus SCE (Ti $-$ 2e $\rightarrow$ Ti^{2+}). The oxidation potential of PPy at the doping process is approximate 0.5 V versus SCE (PPy $-$ e $+$ ClO$_4^-$ $\rightarrow$ PPy$^+$ClO$_4^-$). PPy/Ti could conduct reversible doping–dedoping process of PPy rather than the electrochemical oxidation of the Ti substrate in the potential range of 0~0.8 V. Additionally, the PPy covering layer could also resist such electrochemical corrosion reaction of Ti substrate. Meanwhile, PPy could conduct the redox reaction through the reversible doping–dedoping ClO$_4^-$ anion, contributing to improving the electrochemical activity and, accordingly, the Faradaic capacitance performance.

Figure 4A,B shows the GCD curves of LiClO$_4$/Ti and LiClO$_4$-PPy/Ti in the potential range of 0~0.8 V (vs. SCE) and 1.0 M LiClO$_4$ electrolyte solution. The GCD curves of LiClO$_4$/Ti show complete symmetric characteristics. This shows the good reversible properties of LiClO$_4$ ion adsorption–desorption during the charge–discharge process. Such LiClO$_4$/Ti exhibits ideal electrical double-layer capacitance behavior. Comparatively, the GCD curves of LiClO$_4$-PPy/Ti shows the sloping plateau. The less-symmetric characteristic is ascribed to the redox reaction in the charge–discharge process. Such LiClO$_4$-PPy/Ti exhibits Faradaic capacitance behavior. Therefore, LiClO$_4$-PPy/Ti demonstrates much higher capacitance performance than LiClO$_4$/Ti in the neutral LiClO$_4$ electrolyte. Fur-

thermore, LiClO$_4$-PPy/Ti conducts the doping–dedoping reaction of PPy, and LiClO$_4$/Ti conducts the ion adsorption–desorption process of Ti. The GCD curve shape of LiClO$_4$-PPy/Ti shows fewer identical characteristics than that of LiClO$_4$/Ti. Figure 4C,D shows GCD-based capacitance curves of LiClO$_4$/Ti and LiClO$_4$-PPy/Ti. According to the GCD curves at current densities of 0.01~0.10 mA cm^{-2}, the corresponding GCD-based specific capacitances achieve 0.010~0.0095 mF cm^{-2} and 0.123~0.0122 mF cm^{-2}. Therefore, LiClO$_4$-PPy/Ti exhibits much higher capacitance than LiClO$_4$/Ti, since electroactive LiClO$_4$-PPy mostly contributes to Faradaic capacitance rather than electrical double layer capacitance of Ti substrate in LiClO$_4$ electrolyte. These GCD measurement results agree with the CV measurement results. Furthermore, this LiClO$_4$-PPy/Ti electrode keeps the similar capacitance performance in comparison with the ion doped PPy reported in the literature [36,37]. Figure 4E shows the cycling capacity retention curve of LiClO$_4$-PPy/Ti. The capacity retention achieves 76.1% after 1000 cycles during the cycling charge–discharge process. Therefore, the PPy/Ti electrode exhibits the reasonable cycling stability in the electrochemical Faradaic reaction process.
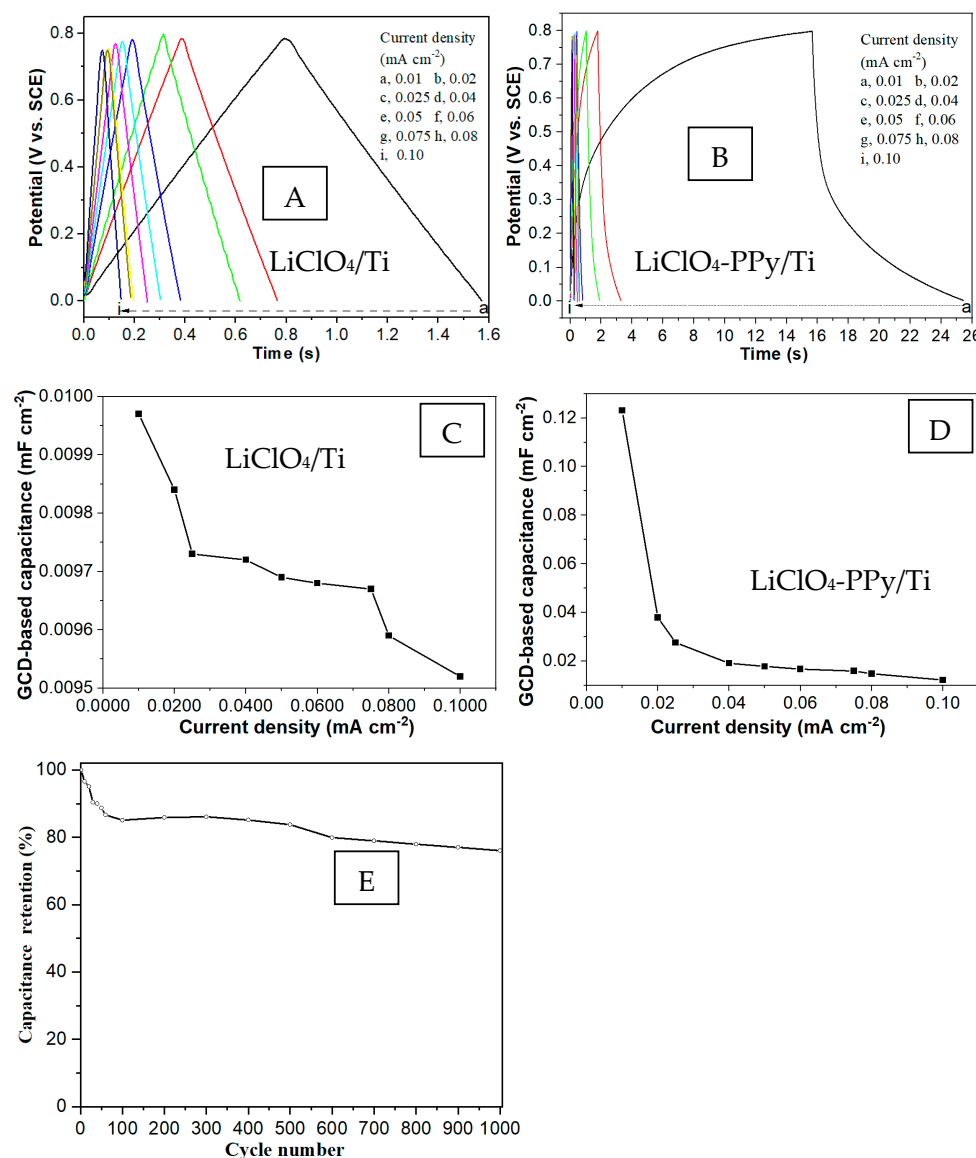

Figure 4. (**A**,**B**) GCD curves and (**C**,**D**) specific capacitance curves of LiClO$_4$/Ti and LiClO$_4$-PPy/Ti at current densities of 0.01~0.1 mA cm^{-2} in 1.0 M LiClO$_4$ electrolyte solution; and (**E**) the cycling capacity retention curve of LiClO$_4$-PPy/Ti.

An electrochemical impedance spectroscopy (EIS) is adopted to investigate the electrolyte ion diffusion and interfacial charge transfer properties of electrode materials. Figure 5A,B shows the Nyquist plots of the EIS spectra of $LiClO_4/Ti$ and $LiClO_4$-PPy/Ti. Figure 5C shows equivalent circuit model for fitting curves of EIS spectra. The equivalent circuit includes charge-transfer resistance (R_{ct}), ohmic resistance (R_o), double layer capacitance (C_{dl}), constant phase element (CPE), and CPE exponent (n). n = 1 indicates ideal capacitor behavior, and n = 0 indicates pure resistor behavior. Table 1 lists the fitting parameter values of these elements used in an equivalent circuit model. In comparison with $LiClO_4/Ti$, the slightly lowered R_o value of $LiClO_4$-PPy/Ti indicates higher electronic conductivity. The ohm resistance of $LiClO_4$-PPy/Ti is mostly dependent on the Ti substrate. The conducting $LiClO_4$-PPy layer prevents the formation of semi-conducting titanium oxide. The quite lowered R_{ct} value indicates the more electroactive interface of $LiClO_4$-PPy for the charge transfer. Its higher C_{dl} value indicates higher double-layer capacitance due to the rougher surface of PPy/Ti rather than Ti substate. However, its higher CPE value indicates the higher Warburg impedance in view of electrolyte diffusion. The Warburg impedance of Ti substrate keeps relatively low value. The lithium ion has relatively high diffusion coefficient and plays a more predominant role than the electrode materials in the $LiClO_4$ electrolyte. $LiClO_4/Ti$ carries out a shorter ion diffusion length than $LiClO_4$-PPy/Ti. Therefore, $LiClO_4/Ti$ reveals a relatively lower CPE value than $LiClO_4$-PPy/Ti. Moreover, $LiClO_4$-PPy/Ti exhibits a larger CPE exponent (n value) than $LiClO_4/Ti$. This indicates that $LiClO_4$-PPy/Ti more likely approaches capacitor behavior rather than resistance behavior. The $LiClO_4$-PPy layer provides more active interface for electrolyte ion adsorption and charge transfer. Therefore, $LiClO_4$-PPy/Ti exhibits higher electroactivity than $LiClO_4/Ti$, contributing to a higher specific capacitance in neutral $LiClO_4$ electrolyte solution.
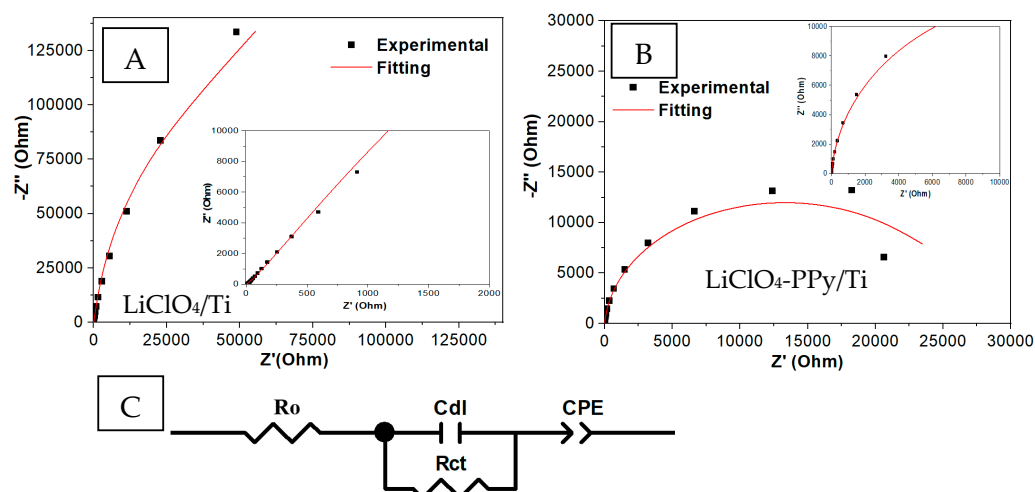

Figure 5. (**A**,**B**) Nyquist plots of EIS spectra of $LiClO_4/Ti$ and $LiClO_4$-PPy/Ti.; and (**C**) equivalent circuit model used for fitting curves of EIS spectra.

Table 1. Fitting parameter values of elements used in equivalent circuit model of $LiClO_4/Ti$ and $LiClO_4$-PPy/Ti.

Substance	C_{dl} (mF cm^{-2})	R_{ct} (Ω cm^{-2})	R_o (Ω cm^{-2})	CPE (S s^n cm^{-2})	n
$LiClO_4/Ti$	0.0334	65,250	0.3660	0.00263	0.746
$LiClO_4$-PPy/Ti	0.1930	2116	0.2226	0.03427	0.912

2.3. DFT Simulation Calculation of $LiClO_4/Ti$ and $LiClO_4$-PPy/Ti

The $LiClO_4$ molecule conducts the adsorption–desorption to establish interfacial interaction between $LiClO_4$ and Ti substrate through Van der Waals forces in the electrochemical

process. The $LiClO_4$ molecule also conducts the doping–dedoping process to establish electrostatic interaction between $LiClO_4$-PPy and Ti substrate. The atomic charge distribution could affect the interaction of $LiClO_4$/Ti and $LiClO_4$-PPy/Ti. The DFT simulation calculation is used to investigate electronic properties of $LiClO_4$/Ti and $LiClO_4$-PPy/Ti [38].

Figure 6A,B shows molecule the structure models of $LiClO_4$/Ti and $LiClO_4$-PPy/Ti. $LiClO_4$/Ti involves an interfacial electrostatic interaction between the $LiClO_4$ and Ti substrate. $LiClO_4$-PPy/Ti involves an interfacial electrostatic interaction between the $LiClO_4$-PPy and Ti substrate. $LiClO_4$-PPy presents the perchlorate ion doping state of PPy.

Figure 6C,D shows the molecular electrostatic potentials of $LiClO_4$/Ti and $LiClO_4$-PPy/Ti. Concerning $LiClO_4$/Ti, the negative charge of ClO_4^- ion could induce the charge dissociation of the Ti substrate, which leads to forming positive and negative crystal lattice Ti atoms. Concerning $LiClO_4$-PPy/Ti, the doping state of $LiClO_4$-PPy reveals a positive charge of hydrogen atoms and negative charge of conjugated pyrrole rings, which leads to the forming of a positive and negative crystal lattice of Ti atoms. The intermolecular interaction distance is determined to be 3.537 Å for perchlorate O...Ti of $LiClO_4$/Ti and 2.450 Å for pyrrole N...Ti of $LiClO_4$-PPy/Ti, respectively. Therefore, $LiClO_4$-PPy/Ti presents stronger electrostatic interaction than $LiClO_4$/Ti. The electrostatic interaction is allowed to occur for $LiClO_4$/Ti and $LiClO_4$-PPy/Ti. The intensified interaction has been established between the $LiClO_4$-PPy molecule chain and the Ti substrate, contributing to the activation of the $LiClO_4$-PPy/Ti electrode.

Figure 6E,F shows the density of states curves of $LiClO_4$/Ti and $LiClO_4$-PPy/Ti. Both $LiClO_4$/Ti and $LiClO_4$-PPy/Ti demonstrate metal conductivity characteristics, since the characteristic density of states at Fermi energy 0 eV cross from the valance band to the conduction band. Comparatively, $LiClO_4$-PPy/Ti demonstrates more orbit energy levels than the $LiClO_4$/Ti at valence band and conduction band regions, which are ascribed to the interfacial interaction between the $LiClO_4$-PPy and the Ti substrate. Furthermore, $LiClO_4$-PPy/Ti shows a higher DOS level (57.321 electrons/eV) than $LiClO_4$/Ti (9.652 electrons/eV) at Fermi energy 0 eV. $LiClO_4$-PPy/Ti exhibits higher electron states and higher electronic conductivity.

Figure 6G,H shows the band gap structure curves of $LiClO_4$/Ti and $LiClO_4$-PPy/Ti. The band gaps of $LiClO_4$/Ti and $LiClO_4$-PPy/Ti approach 0.03 and 0 eV, presenting similar superior conductivity of metal substrates. Comparatively, $LiClO_4$-PPy/Ti demonstrates much greater energy levels at the valance band and conduction band regions than $LiClO_4$/Ti, which presents superior electrical conductivity of $LiClO_4$-PPy/Ti. Therefore, the band gap analysis results agree with the DOS analysis results, proving the superior electronic conductivity of $LiClO_4$-PPy/Ti rather than $LiClO_4$/Ti. The declined interfacial energies are -5.202×10^3 eV for $LiClO_4$/Ti and -1.461×10^4 for $LiClO_4$-PPy/Ti, which presents the intensified interfacial interaction of $LiClO_4$-PPy/Ti. Therefore, $LiClO_4$-PPy/Ti shows higher electroactivity than $LiClO_4$/Ti. $LiClO_4$-PPy has more electronic distribution than $LiClO_4$-PPy/Ti, which leads to stronger interaction, lower interfacial energy, and, accordingly, higher capacitance performance.

Figure 6I shows the HOMO and LUMO HOMO and LUMO frontier molecular orbital charge distribution of $LiClO_4$/Ti and $LiClO_4$-PPy/Ti. Concerning HOMO and LUMO electron distribution in $LiClO_4$/Ti and $LiClO_4$-PPy/Ti, their molecular orbitals are mostly dependent on Ti rather than $LiClO_4$ and $LiClO_4$-PPy. In Ti atoms, there occurs an obvious electronic transition, which causes heterogeneous electron distribution. Comparatively, different O and Cl atoms in $LiClO_4$ occur insignificant electronic transition due to weak electron transfer. Similarly, the electron transition of different atoms in $LiClO_4$-PPy also becomes relatively neglective because of weak electronic transfer. The HOMO-LUMO molecule orbital energy gaps of $LiClO_4$/Ti and $LiClO_4$-PPy/Ti are determined to be 0.340 eV and 0.032 eV, respectively. Therefore, $LiClO_4$-PPy/Ti with a low HOMO-LUMO gap presents its high conductivity and high electroactivity, also. The HOMO-LUMO gap analysis results agree with the DOS and band gap analysis results. The DFT simulation

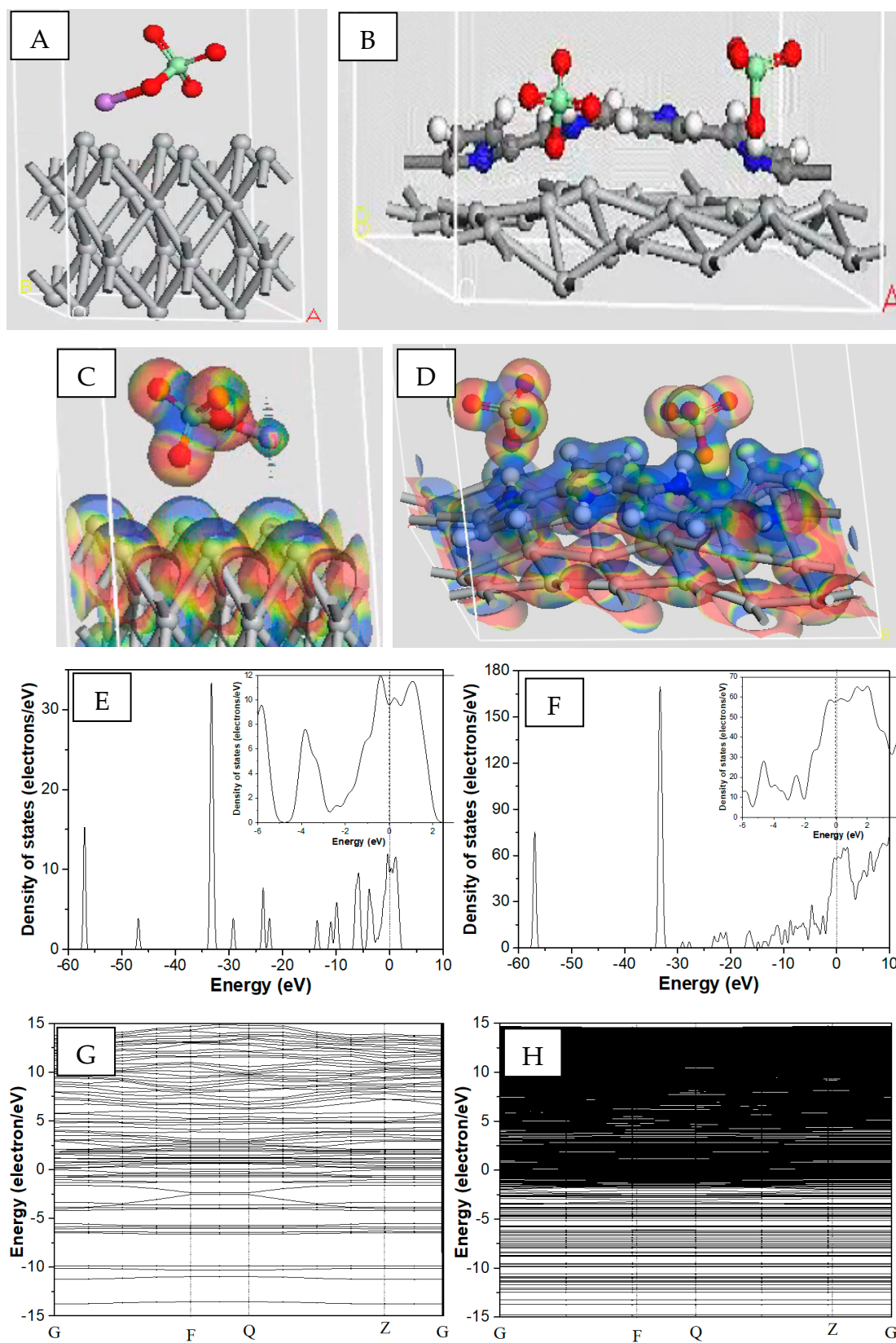calculation results support the CV and GCD measurement results, proving the higher capacitance of LiClO$_4$-PPy/Ti.
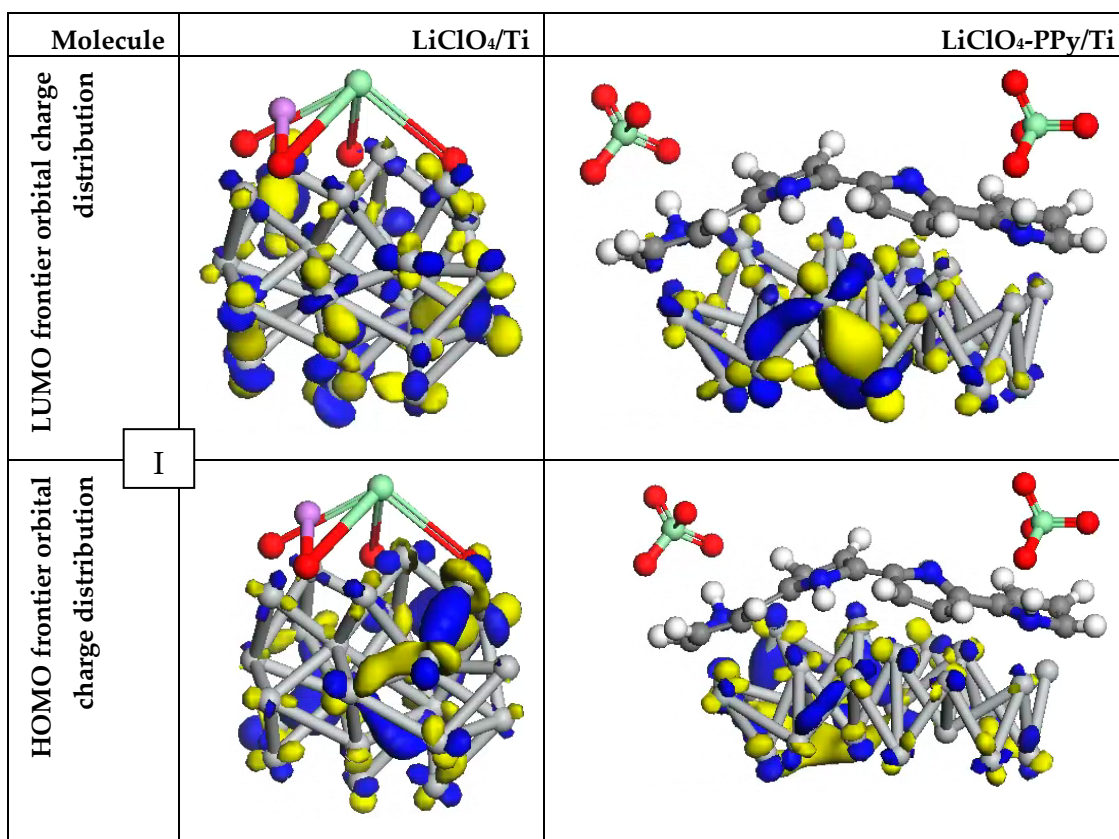

Figure 6. *Cont.*

Molecule	LiClO₄/Ti	LiClO₄-PPy/Ti
LUMO frontier orbital charge distribution		
I		
HOMO frontier orbital charge distribution		

Figure 6. (**A**,**B**) Molecule structure models, (**C**,**D**) molecular electrostatic potentials (difference charge density), (**E**,**F**) total density of states curves, (**G**,**H**) band gap structure curves, (**I**) HOMO and LUMO frontier molecular orbital charge distribution of LiClO₄/Ti and LiClO₄-PPy/Ti.

Figure 7 shows the Mulliken charge population of C, O, N, Cl, and Ti atoms of LiClO₄/Ti and LiClO₄-PPy/Ti. The interfacial interaction in LiClO₄/Ti and LiClO₄-PPy/Ti leads to the center charge offset of the Ti lattice atoms and the negative charge density distribution of oxygen atoms as well as nitrogen atoms. Accordingly, Ti atoms involve the dissociation distribution of negative and positive charge in LiClO₄/Ti and LiClO₄-PPy/Ti. Table 2 lists the Mulliken charges of C, O, N, Cl, and Ti atoms in LiClO₄/Ti and LiClO₄-PPy/Ti. The negative charge densities of oxygen atoms are changed from LiClO₄/Ti (−0.78, −0.80, −0.82, −0.95) to LiClO₄-PPy/Ti (−0.76, −0.77, −0.78, −0.90), indicating a slightly decreased negative charge. The dissociated positive and negative charge densities of Ti substrate are (+0.13~+0.05)/(−0.23~−0.04) for LiClO₄/Ti and (+0.62~+0.08)/(−0.05~−0.01) for LiClO₄-PPy/Ti, respectively. Therefore, the electrostatic interaction is formed between negative-charged perchlorate O and positive-charged Ti. Additionally, the negative charge densities of nitrogen atom are (−0.58~−0.47). Obviously, the strong electrostatic interaction is further formed between the negative-charged pyrrole N and the positive-charged Ti in LiClO₄-PPy/Ti. Herein, LiClO₄ exhibits the surface adsorption state of Ti in LiClO₄/Ti and the doping state of PPy in LiClO₄-PPy/Ti. The Mulliken charge population analysis proves the shorter intermolecular interaction distance in LiClO₄-PPy/Ti in comparison with LiClO₄/Ti. Accordingly, LiClO₄-PPy/Ti achieves higher electroactivity than LiClO₄/Ti. The DFT simulation calculation results agree with the experimental measurement results in confirming the superior capacitance of LiClO₄-PPy/Ti.
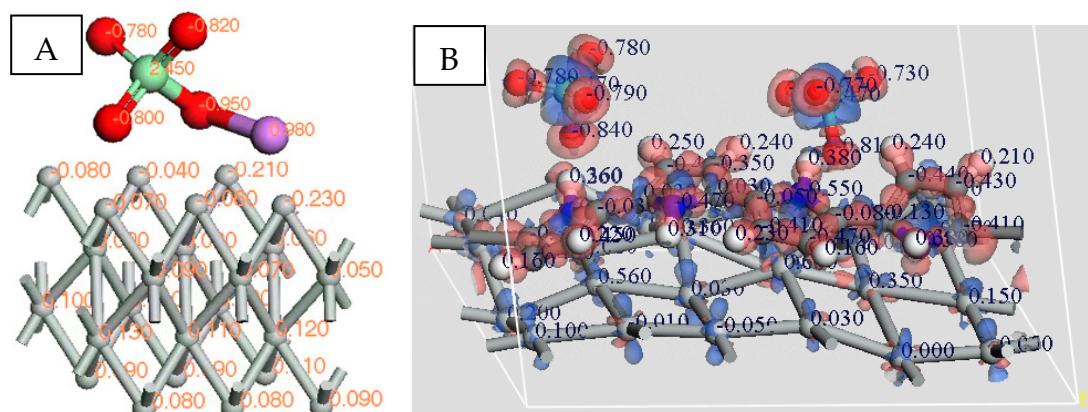
Figure 7. Mulliken charge population of (**A**) LiClO$_4$/Ti and (**B**) LiClO$_4$-PPy/Ti.

Table 2. Mulliken charge population of C, O, N, Cl, and Ti atoms in LiClO$_4$/Ti and LiClO$_4$-PPy/Ti.

Element	LiClO$_4$-Ti	LiClO$_4$-PPy-Ti
O1	−0.78	−0.76
O2	−0.80	−0.77
O3	−0.82	−0.78
O4	−0.95	−0.90
Cl	+2.45	+2.47
C1	/	+0.03
C2	/	+0.04
N	/	(−0.58~−0.47)
Ti	(−0.23~−0.04) (+0.13~+0.05)	(−0.05~−0.01) (+0.62~+0.08)

3. Experimental Section

3.1. Preparation of LiClO$_4$-PPy/Ti

The titanium sheet (Ti, purity 99.5%, size 10×50 mm, thickness 0.2 mm.) was washed using acetone, ethanol, and then deionized water to remove surface stains. The Ti sheet then conducted the chemical polishing treatment in HF-HNO$_3$ solution to dissolve the surface-covered oxide layer. The chemical cleaned Ti sheet was obtained. The Ti sheet conducted the electrostatic adsorption in lithium perchlorate solution form LiClO$_4$/Ti. A normal pulse voltammetry process was employed to synthetize LiClO$_4$-PPy/Ti using a three-electrode reaction system, which included the fresh Ti sheet working electrode, Pt foil counter electrode, the Hg/Hg$_2$Cl$_2$ reference electrode, and acetonitrile solvent solution of 0.1 M LiClO$_4$ electrolyte and 0.15 M pyrrole. The reaction parameters included a pulse potential range of 0.7~1.1 V and pulse potential increment of 0.001 V.

3.2. Characterization and Measurement

The surface microstructure characterization of LiClO$_4$-PPy/Ti and LiClO$_4$/Ti was conducted using a scanning electron microscope (SEM, ZEISS Ultra Plus, Germany). A Raman spectrum measurement of LiClO$_4$-PPy/Ti was conducted using a Raman spectroscope (Thermo Fisher DXR3, He-Ne laser, Emitting wavelength of 785 nm). A crystal phase structure characterization of titanium substrate was conducted using an X-ray diffraction (XRD, Bruker D8-Discover, Wavelength of X-ray source, 0.154 nm) apparatus. Electrochemical capacitive measurements of LiClO$_4$-PPy/Ti and LiClO$_4$/Ti were performed using an electrochemical workstation (CHI 760D, CH Instruments Co., Ltd., China), which includes galvanostatic charge/discharge (GCD) and cyclic voltammetry (CV). The electrochemical impedance spectrum (EIS) measurement was carried out at the frequency range of 10^{-2}~10^5 Hz. The 1.0 M LiClO$_4$ was used as the doping ion source and the electrolyte solution, contributing to maintaining the electrochemical stability of the titanium substrate

in LiClO$_4$-PPy/Ti. electrode. The total surface area was used to evaluate electrochemical capacitance.

3.3. Theoretical Simulation Calculation

Density functional theory (DFT) simulation calculation was carried out to investigate electronic properties and atomic charge distribution of LiClO$_4$ and LiClO$_4$-PPy interaction at the interface of Ti substrate [38]. The total density of states (DOS), Mulliken charge population, interfacial binding energy, highest occupied molecular orbital (HOMO), lowest unoccupied molecular orbital (LUMO), and electrostatic potential were determined and discussed for better understanding of the electrostatic interfacial interaction of LiClO$_4$-PPy/Ti and LiClO$_4$/Ti. The DMol3 package was applied to calculate HOMO-LUMO energy gaps, and the CASTEP package was applied to calculate electronic energy gap and charge density difference and DOS value.

4. Conclusions

The PPy/Ti has been prepared through an electro-polymerization deposition process which is applied as supercapacitor electrode for electrochemical energy storage. Theoretical and experimental investigations are adopted to disclose the conductivity and interfacial interaction-dependent capacitance of LiClO$_4$-PPy/Ti. LiClO$_4$/Ti reveals ideal electrical double-layer capacitance due to the reversible adsorption/desorption of LiClO$_4$ electrolyte on Ti substrate in the potential range of 0~0.8 V. LiClO$_4$-PPy/Ti reveals Faradaic capacitance due to reversible doping/dedoping perchlorate ion in PPy. LiClO$_4$-PPy/Ti reveals lower charge transfer resistance, lower ohmic resistance, and lower Warburg resistance to present more active interface, higher electronic conductivity, and more feasible ion diffusion properties than LiClO$_4$/Ti. LiClO$_4$/Ti and LiClO$_4$-PPy/Ti achieve the mean response current of 0.13~2.47 μA cm^{-2} and 2.28~9.011 μA cm^{-2} at 5~200 mV s^{-1}. The corresponding specific capacitances are 0.010~0.0095 mF cm^{-2} and 0.123~0.0122 mF cm^{-2} at 0.01~0.10 mA cm^{-2}. LiClO$_4$-PPy/Ti keeps much higher electrochemical conductivity and higher specific capacitance than LiClO$_4$/Ti. Theoretical calculation results prove that interfacial electrostatic adsorption of LiClO$_4$/Ti and ClO$_4^-$ anion doping of LiClO$_4$-PPy/Ti could change atomic charge density distribution. LiClO$_4$-PPy/Ti exhibits higher electronic conductivity and lower interface energy than LiClO$_4$/Ti. LiClO$_4$-PPy/Ti can act as a superior supercapacitor electrode to exhibit electroactivity and capacitance for the promising energy storage application.

Author Contributions: Formal analysis, Y.X. and J.X.; data curation, Y.X., L.L. and C.X.; writing—original draft preparation, Y.X.; writing—review and editing, Y.X. All authors have read and agreed to the published version of the manuscript.

Conflicts of Interest: The authors declare no conflicts of interest.

References

1. Chen, G.Z. Understanding supercapacitors based on nano-hybrid materials with interfacial conjugation. *Prog. Natl. Sci.* **2013**, *23*, 245–255. [CrossRef]
2. Adalati, R.; Sharma, M.; Sharma, S.; Kumar, A.; Malik, G.; Boukherroub, R.; Chandra, R. Metal nitrides as efficient electrode material for supercapacitors: A review. *J. Energy Stor.* **2022**, *56*, 105912. [CrossRef]
3. Yadav, M.S. Metal oxides nanostructure-based electrode materials for supercapacitor application. *J. Nanopart. Res.* **2020**, *22*, 367. [CrossRef]
4. Parveen, N.; Ansari, S.A.; Ansari, M.Z.; Ansari, M.O. Manganese oxide as an effective electrode material for energy storage: A review. *Environ. Chem. Lett.* **2022**, *20*, 283–309. [CrossRef]

5. Ansari, M.Z.; Nandi, D.K.; Janicek, P.; Ansari, S.A.; Ramesh, R.; Cheon, T.; Shong, B.; Kim, S.-H. Low-Temperature Atomic Layer Deposition of Highly Conformal Tin Nitride Thin Films for Energy Storage Devices. *Acs Appl. Mater. Interface* **2019**, *11*, 43608–43621. [CrossRef]

6. Parveen, N.; Hilal, M.; Han, J.I. Newly Design Porous/Sponge Red Phosphorus@Graphene and Highly Conductive Ni_2P Electrode for Asymmetric Solid State Supercapacitive Device with Excellent Performance. *Nano-Micro Lett.* **2020**, *12*, 25. [CrossRef] [PubMed]

7. Karnan, M.; Hari Prakash, K.; Badhulika, S. Revealing the super capacitive performance of N-doped hierarchical porous activated carbon in aqueous, ionic liquid, and redox additive electrolytes. *J. Energy Stor.* **2022**, *53*, 105189. [CrossRef]

8. Xie, Y. Electrochemical Performance of Polyaniline Support on Electrochemical Activated Carbon Fiber. *J. Mater. Eng. Perform.* **2022**, *31*, 1949–1955. [CrossRef]

9. Wang, H.; Xie, Y. Hydrogen bond enforced polyaniline grown on activated carbon fibers substrate for wearable bracelet supercapacitor. *J. Energy Stor.* **2022**, *52*, 105042. [CrossRef]

10. Xie, Y. Electrochemical and hydrothermal activation of carbon fiber supercapacitor electrode. *Fiber Polym.* **2022**, *23*, 10–17. [CrossRef]

11. Xie, Y.; Wang, Y.; Wang, L.; Liang, J. Theoretical and Experimental Investigations of Oxygen Activation Effect of Carbon Nanofibers Interacting with Polypyrrole. *Fibers* **2024**, *12*, 4. [CrossRef]

12. Zhai, Z.; Zhang, L.; Du, T.; Ren, B.; Xu, Y.; Wang, S.; Miao, J.; Liu, Z. A review of carbon materials for supercapacitors. *Mater. Des.* **2022**, *221*, 111017. [CrossRef]

13. Jáquez-Muñoz, J.M.; Gaona-Tiburcio, C.; Chacón-Nava, J.; Cabral-Miramontes, J.; Nieves-Mendoza, D.; Maldonado-Bandala, E.; Delgado, A.D.; Flores-De los Rios, J.P.; Bocchetta, P.; Almeraya-Calderón, F. Electrochemical Corrosion of Titanium and Titanium Alloys Anodized in H_2SO_4 and H_3PO_4 Solutions. *Coatings* **2022**, *12*, 325. [CrossRef]

14. Ansari, S.A.; Khan, N.A.; Hasan, Z.; Shaikh, A.A.; Ferdousi, F.K.; Barai, H.R.; Lopa, N.S.; Rahman, M.M. Electrochemical synthesis of titanium nitride nanoparticles onto titanium foil for electrochemical supercapacitors with ultrafast charge/discharge. *Sustain. Energy Fuels* **2020**, *4*, 2480–2490. [CrossRef]

15. Liu, X.Y.; Chen, H.; Li, G.; Peng, J.H.; Zhang, Y.X. One-pot synthesis of pearl-chain-like manganese dioxide-decorated titanium grids as advanced binder-free supercapacitors electrodes. *Ceram. Int.* **2016**, *42*, 9227–9233. [CrossRef]

16. Wang, L.; Ma, Y.; Yang, M.; Qi, Y. Titanium plate supported MoS_2 nanosheet arrays for supercapacitor application. *Appl. Surf. Sci.* **2017**, *396*, 1466–1471. [CrossRef]

17. Wei, J.; Wei, S.; Wang, G.; He, X.; Gao, B.; Zhao, C. PPy modified titanium foam electrode with high performance for supercapacitor. *Eur. Polym. J.* **2013**, *49*, 3651–3656. [CrossRef]

18. Zhang, J.; Yu, X.; Zhao, Z.-y.; Zhang, Z.; Li, J. Influence of pore size of Ti substrate on structural and capacitive properties of Ti/boron doped diamond electrode. *J. Alloys Compd.* **2019**, *777*, 84–93. [CrossRef]

19. Chang, L.; Chen, B.; Qiao, H.; Huang, H.; Guo, Z.; He, Y.; Xu, R.; Xionghui, X. Study of the Effects of Pretreatment Processing on the Properties of Metal Oxide Coatings on Ti-Based Sheet. *J. Electrochem. Soc.* **2021**, *168*, 033501. [CrossRef]

20. Kishimoto, A.; Yamada, Y.; Funatsu, K.; Uda, T. Suitable Electrode Materials for Titanium Sheet Deposition. *Adv. Eng. Mater.* **2020**, *22*, 1900747. [CrossRef]

21. Lamberti, A. Flexible supercapacitor electrodes based on MoS_2-intercalated rGO membranes on Ti mesh. *Mater. Sci. Semicond. Process.* **2018**, *73*, 106–110. [CrossRef]

22. Seo, H.-S.; Bae, J.-U.; Kim, D.-H.; Park, Y.; Kim, C.-D.; Kang, I.B.; Chung, I.-J.; Choi, J.-H.; Myoung, J.-M. Reliable Bottom Gate Amorphous Indium-Gallium-Zinc Oxide Thin-Film Transistors with TiO_x Passivation Layer. *Electrochem. Solid State Lett.* **2009**, *12*, H348–H351. [CrossRef]

23. Reddy, P.C.H.; Amalraj, J.; Ranganatha, S.; Patil, S.S.; Chandrasekaran, S. A review on effect of conducting polymers on carbon-based electrode materials for electrochemical supercapacitors. *Synth. Met.* **2023**, *298*, 117447. [CrossRef]

24. Tsekova, D.S.; Karastoyanov, V.; Peychev, D.; Valova, I. Crystallization of ferritin on biocompatible Surfaces—Bare Ti and Ti covered by polypyrrole (PPy). *J. Cryst. Growth* **2024**, *631*, 127616. [CrossRef]

25. Chen, J.; He, Y.; Li, L. Real-time probing electrodeposition growth of polyaniline thin film via in-situ spectroscopic ellipsometry. *Thin Solid Films* **2022**, *762*, 139565. [CrossRef]

26. Kondratiev, V.V.; Holze, R. Intrinsically conducting polymers and their combinations with redox-active molecules for rechargeable battery electrodes: An update. *Chem. Pap.* **2021**, *75*, 4981–5007. [CrossRef]

27. Stejskal, J.; Sapurina, I.; Vilčáková, J.; Humpolíček, P.; Truong, T.H.; Shishov, M.A.; Trchová, M.; Kopecký, D.; Kolská, Z.; Prokeš, J.; et al. Conducting polypyrrole-coated macroporous melamine sponges: A simple toy or an advanced material? *Chem. Pap.* **2021**, *75*, 5035–5055. [CrossRef]

28. Ji, S.; Yang, J.; Cao, J.; Zhao, X.; Mohammed, M.A.; He, P.; Dryfe, R.A.W.; Kinloch, I.A. A Universal Electrolyte Formulation for the Electrodeposition of Pristine Carbon and Polypyrrole Composites for Supercapacitors. *Acs Appl. Mater. Interface* **2020**, *12*, 13386–13399. [CrossRef] [PubMed]

29. Zhu, H.; Xie, Y. Electrochemical performance of bridge molecule-reinforced activated carbon fiber-m-aminobenzenesulfonic acid-polyaniline for braidable-supercapacitor application. *Chem. Eng. J.* **2023**, *478*, 147416. [CrossRef]

30. Jakhar, P.; Shukla, M.; Singh, V. Influence of $LiClO_4$ Concentration on 1-D Polypyrrole Nanofibers for Enhanced Performance of Glucose Biosensor. *J. Electrochem. Soc.* **2018**, *165*, G80–G89. [CrossRef]

31. Santino, L.M.; Acharya, S.; D'Arcy, J.M. Low-temperature vapour phase polymerized polypyrrole nanobrushes for supercapacitors. *J. Mater. Chem. A* **2017**, *5*, 11772–11780. [CrossRef]

32. Sharifi-Viand, A.; Mahjani, M.G.; Moshrefi, R.; Jafarian, M. Diffusion through the self-affine surface of polypyrrole film. *Vacuum* **2015**, *114*, 17–20. [CrossRef]

33. Wysocki, B.; Maj, P.; Sitek, R.; Buhagiar, J.; Kurzydłowski, K.J.; Święszkowski, W. Laser and Electron Beam Additive Manufacturing Methods of Fabricating Titanium Bone Implants. *Appl. Sci.* **2017**, *7*, 657. [CrossRef]

34. Hasoon, S. Electrochemical polymerization and Raman study of polypyrrole and polyaniline thin films HS Abdullah. *Int. J. Phys. Sci.* **2012**, *7*, 5468–5476.

35. Fernández Romero, A.J.; López Cascales, J.J.; Fernández Otero, T. Perchlorate Interchange during the Redox Process of PPy/PVS Films in an Acetonitrile Medium. A Voltammetric and EDX Study. *J. Phys. Chem. B* **2005**, *109*, 907–914. [CrossRef] [PubMed]

36. Wang, J.; Wu, C.; Wu, P.; Li, X.; Zhang, M.; Zhu, J. Polypyrrole capacitance characteristics with different doping ions and thicknesses. *Phys. Chem. Chem. Phys.* **2017**, *19*, 21165–21173. [CrossRef] [PubMed]

37. Chen, S.; Liu, H.; Wang, Y.; Xu, S.; Liu, W.; He, D.; Liu, X.; Liu, J.; Hu, C. Electrochemical Capacitance of Spherical Nanoparticles Formed by Electrodeposition of Intrinsic Polypyrrole onto Au Electrode. *Electrochim. Acta* **2017**, *232*, 72–79. [CrossRef]

38. Xie, Y.; Mu, Y. Interface Mo-N coordination bonding MoSxNy@Polyaniline for stable structured supercapacitor electrode. *Electrochim. Acta* **2021**, *391*, 138953. [CrossRef]